Large Magnetoresistance in Magnetically Coupled $SrRuO_3$ –$CoFe_2O_4$ Self-Assembled Nanostructures

*Heng-Jui Liu, Vu-Thanh Tra, Ying-Jiun Chen, Rong Huang, Chun-Gang Duan, Ying-Hui Hsieh, Hong-Ji Lin, Jiunn-Yuan Lin, Chien-Te Chen, Yuichi Ikuhara, and Ying-Hao Chu**

Interface couplings in self-assembled nanostructures, especially in complex oxide composites, have been considered as a powerful tool to create and manipulate the lattice, charge, orbital, and spin degrees of freedoms.[1,2] Among various nanocomposites, vertical heteroepitaxial nanostructures with a high interface-to-volume ratio have become some of the most attractive systems because of their superior physical properties and designed functionalities through interfacial coupling, for example, strong and controllable magnetoelectric coupling in combinations of ferroelectric perovskites–ferromagnetic spinels (i.e., $BaTiO_3$ –$CoFe_2O_4$, $BiFeO_3$ –$CoFe_2O_4$, etc.),[3–7] an abnormal dielectric response in $BiFeO_3$ –Sm_2O_3,[8] enhanced ferroelectricity in $BaTiO_3$ –Sm_2O_3,[9] and low magnetic-field driven colossal magnetoresistance (CMR) in manganite-based nanocomposites.[10–13] Our previous work had also manifested that a photon-driven variation of magnetic pillars can be observed in nanostructures composed of photostrictive $SrRuO_3$ (SRO) and magnetostrictive $CoFe_2O_4$ (CFO).[14] This is a very fascinating system since besides the presence of a photomagnetic effect, the transport behavior is another focal point we have tried to disclose. In this system, SRO is a well-known "bad metal" oxide material, of which the resistivity shows a kink at its Curie temperature ($T_{C,SRO}$, ≈150 K for thin film and ≈160 K for bulk).[15] Unlike the perovskite manganites with CMR effect,[16,17] SRO does not show an impressive magnetoresistance (MR), which always requires a large field (above 3 Tesla (T)) and very low temperature (below 10 K) to achieve a value less than 10%.[18–20] CFO is an insulator[21] and can present a large strain-induced magnetic anisotropy while it forms the nanopillars embedded in an SRO matrix.[14] Therefore, our motivation is to create a model system to see how the magnetic nanostructures directly affect the macroscopic transport behavior of the metallic matrix. The findings here are very attractive since they demonstrate that an unanticipated large MR effect (≈40% at 0.5 T) at around the Curie temperature of SRO ($T_{C,SRO}$) can be achieved in this non-manganite-based system. This work delivers a solution to trigger new functionalities in the strongly correlated systems and therefore opens a new pathway to engineer and design the functionalities of heteroepitaxial oxide nanostructures.

The self-assembled vertical heteroepitaxial nanostructures were synthesized via a dual-target method in a pulsed laser deposition process.[14] A typical depiction of the self-assembled nanostructures is illustrated in **Figure 1**a. It shows a clear signature of phase separation, which presents only a CFO peak and SRO peaks in the vicinity of (001) oriented $SrTiO_3$ (STO) peaks (substrate) measured by an X-ray θ–2θ scan (Figure 1b). According to X-ray diffraction (XRD) analysis, the *c*-axis lattice constants of the SRO and CFO are calculated as 3.934 and 8.29 Å, respectively. Compared with the bulk value of pseudo-cubic SRO (a = 3.927 Å)[18] and cubic CFO (a = 8.39 Å),[21] the SRO is almost relaxed and CFO has a large compressive strain along the out-of-plane direction. Our previous work has revealed that this large decrease of the CFO *c*-axis lattice is caused by the interfacial lattice coupling with SRO, and thus leads to a large coercivity and strain-induced anisotropy field due to the magnetostriction of CFO.[14] In order to acquire more structural information, we then investigated the sample by high-angle annular dark-field scanning transmission electron microscopy (HAADF-STEM). It is noted that the nanopillars are embedded in the matrix with a distinguishable contrast from the low-magnification HAADF image. A typical HAADF image showing the nanopillars and nearby matrix is given in the upper panel of Figure 1c. The CFO and SRO can be easily distinguished along the [110] zone axis. The enlarged atomic image captured from the yellow frame in the nanopillar area exhibits a spinel-based structure, consistent with the simulated atomic arrangement of CFO along the [110] direction, as shown in the lower-left

Dr. H.-J. Liu, Y.-H. Hsieh, Prof. Y.-H. Chu
Department of Materials Science and Engineering
National Chiao Tung University
Hsinchu 30010, Taiwan ROC
E-mail: yhc@nctu.edu.tw
V.-T. Tra, Prof. J.-Y. Lin
Institute of Physics
National Chiao Tung University
Hsinchu 30010, Taiwan ROC
Y.-J. Chen, Dr. H.-J. Lin, Dr. C.-T. Chen
National Synchrotron Radiation Research Center
Hsinchu 30010, Taiwan ROC
Prof. R. Huang, Prof. C.-G. Duan
Key Laboratory of Polar Materials and Devices
Ministry of Education
East China Normal University
ShangHai 200241, P. R. China
Prof. R. Huang, Prof. Y. Ikuhara
Nanostructures Research Laboratory
Japan Fine Ceramics Center
Nagoya 456-8587, Japan
Prof. Y. Ikuhara
Institute of Engineering Innovation
the University of Tokyo
Tokyo 113-8656, Japan

DOI: 10.1002/adma.201301461

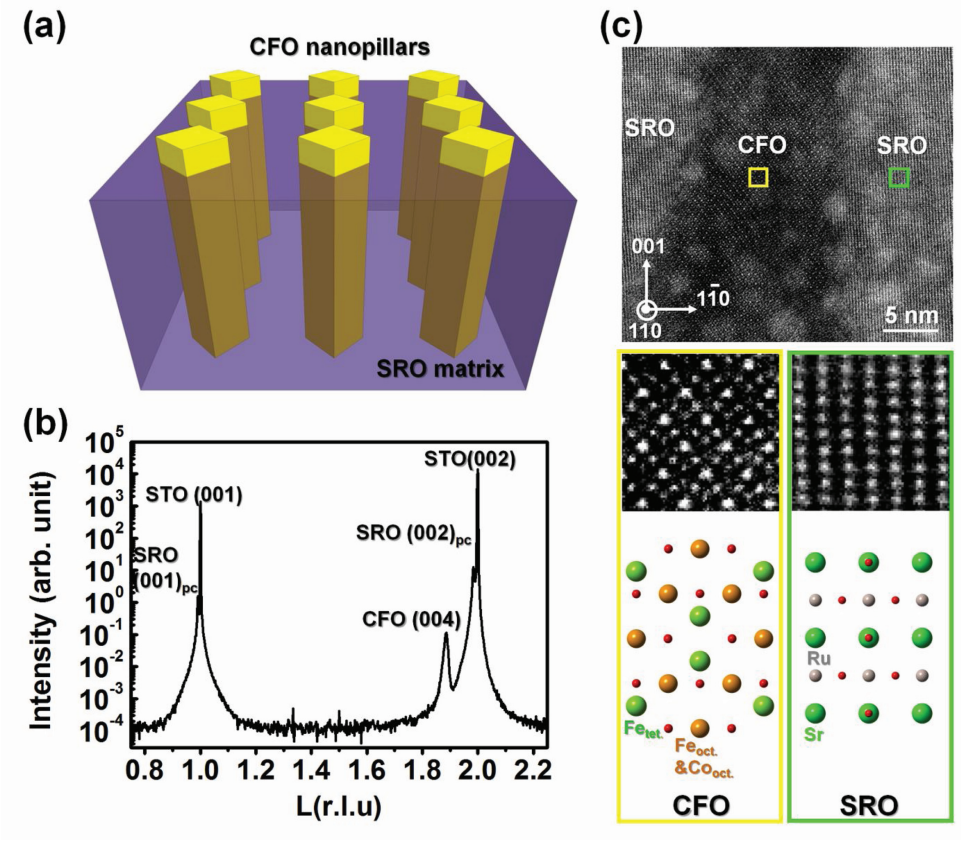

Figure 1. a) A typical depiction of the vertical heteroepitaxial nanocomposites, in which the CFO nanopillars are embedded in an SRO matrix. b) The high resolution θ–2θ XRD pattern of the CFO–SRO nanocomposites. c) The HADDF-STEM image shows an obvious phase-separation. The magnified atomic images obtained from yellow and green squares in the respective regions of the nanopillar and matrix can be identified as CFO and SRO, which present the same atomic arrangement as the simulated patterns.

panel of Figure 1c. However, the enlarged atomic image from the green frame in the matrix area shows different features, which matches with the [110] zone axis of perovskite SRO (the lower-right panel of Figure 1c). Furthermore, the orientation relationships between the CFO nanopillars and SRO matrix are revealed as $(001)_{CFO} \parallel (001)_{SRO}$ and $[110]_{CFO} \parallel [110]_{SRO}$, consistent with the XRD analyses. These results indicate that the self-assembled vertical heteroepitaxial nanostructures of CFO nanopillars and SRO matrix are well synthesized as expected and show good crystal quality.

To probe the transport behaviors of the SRO–CFO system, conductive atomic force microscopy (C-AFM) was first performed to investigate the local conduction on the sample. In **Figure 2**a, the C-AFM image presents a bright contrast in most areas, except for regions where the CFO pillars are located, when a small direct current (DC) voltage (1.2 V) is applied. It clearly illustrates that the SRO matrix is more conducting than the CFO nanopillars. The temperature-dependent resistivity ρ (T) was then measured to characterize the macroscopic transport behavior in this kind of nanostructured film (Figure 2b). The sample B and C were fabricated with the same deposition parameters of sample A to check the reproducibility, and all samples were cooled in a closed cycle refrigeration Quantum Design physical property measurement system (PPMS) from room temperature to 20 K. We found that all the CFO–SRO nanostructured thin films give a semiconducting characteristic, which is very different from the metallic behavior of pure SRO thin films. We then transformed these resistivity curves into conductivity curves and analyzed them in more detail. First, the Arrhenius plots in Figure 2c show that the curve of $\ln(\rho)$ against the inverse of temperature (T^{-1}) can be fitted well by a linear function at the high temperature region (≈90–300 K) using the equation: $\ln(\rho) = \ln(\rho_a) + [-E_A/(k_B T)]$, where k_B = Boltzmann constant. The thermal activation energy (E_A) extracted from the slope (s) of each curve ($s = E_A/k_B$) is around 22 to 27 meV, which is very close to some doping semiconductor systems.[22,23] When the temperature goes below 90 K, the variation of conductivity is not suitable for the thermal activation model anymore. It then coincides with the Mott variable range hopping (Mott VRH) mechanism at the temperature region of around 30 to 95 K, which tallies with an approximate equation: $\ln(\rho) \approx -(T_0/T)^{1/4}$ as shown in Figure 2d. It suggests that the carriers could not move freely and the conduction is dependent on the hopping between localized states near the Fermi level (E_F). These localized carriers, which are possibly a result of the chemical interaction with the CFO pillars, could result in the depressed itinerant Ru 4d electrons since a similar behavior has been discovered in many doped SRO systems.[24–28]

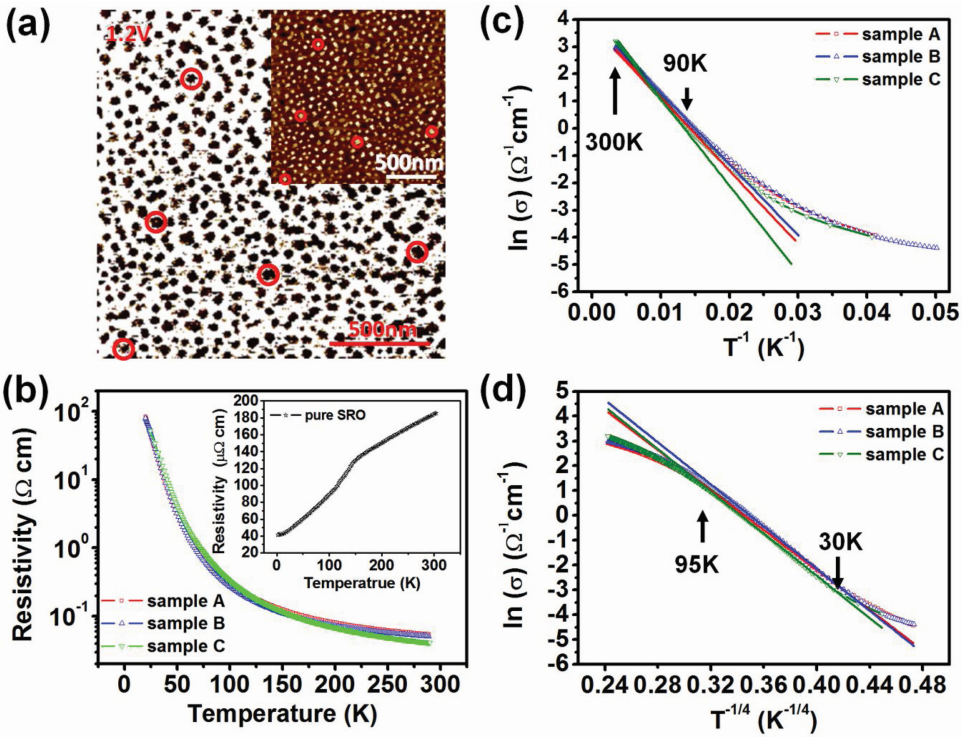

Figure 2. a) The red circles marked in the C-AFM image and the inset of topography confirm that both images are in the same area. The C-AFM image operated at 1.2 V shows a clear contrast which indicates the SRO matrix is more conducting than the CFO nanopillars. b) Sample A was fabricated in a CFO/SRO ratio of 0.33, and B and C are the repeated samples for test of reproducibility. The temperature-dependent transport curves clearly illustrate a semiconducting behavior in these samples rather than a metallic behavior in pure SRO. c,d) The curve-fitting of these samples using the thermal activated model and Mott VRH mechanism, respectively.

In order to reveal the chemical interaction in this system, X-ray energy-dispersive spectroscopy (EDS) analyses were performed in a Cs-corrected STEM. **Figure 3** shows typical EDS mapping of the sample. The features of the CFO nanopillars embedded into the SRO matrix are clearly seen in the distributions of each element. Interestingly, the discernible Fe signals appear in the SRO matrix areas as shown in the Fe map, in contrast to the Co map, where no Co signals were detected in the SRO matrix areas. To confirm this information, two EDS spectra were acquired at the positions of the red dot (CFO

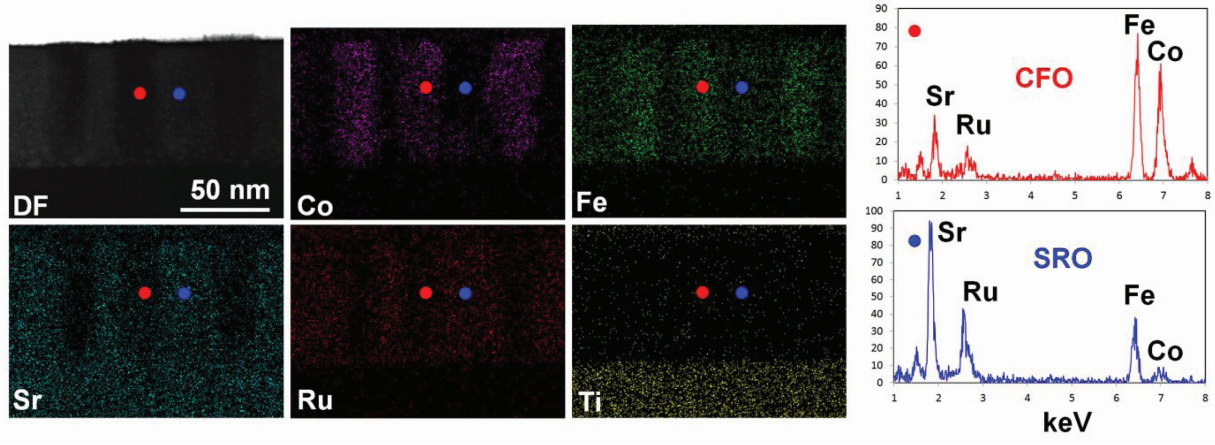

Figure 3. The EDS mapping reveals the distribution of elemental Co, Fe, Sr, Ru, and Ti. Compared with the low-magnification HADDF image, these images also confirm that the pillars are CFO and matrix is SRO. The EDS spectra acquired from the red dot in the nanopillar and blue dot in the matrix reveal that the Co/Fe ratio in the CFO nanopillars is higher than 1/2 (the ratio of standard CFO) and stronger Fe signals than Co were detected in the SRO matrix. This indicates that the Fe atoms from CFO nanopillars have diffused into the SRO matrix and thus leads to the non-stoichiometric Co/Fe ratio in the pillars.

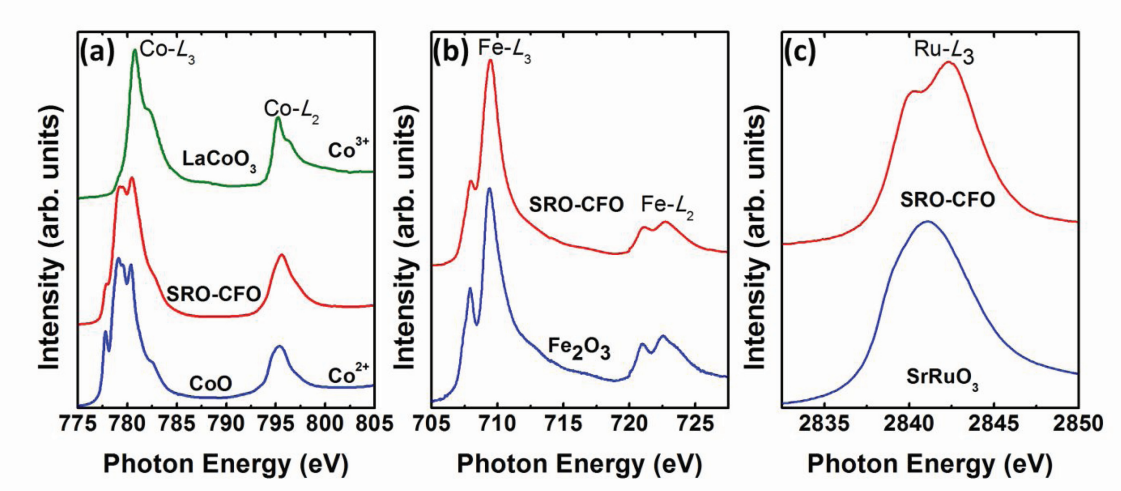

Figure 4. The XAS measurements of the Co-$L_{2,3}$, Fe-$L_{2,3}$, and Ru-L_3 edges: a) The Co spectrum in the SRO–CFO nanostructures compared with the standard sample of $LaCoO_3$ and CoO suggests the presence of a mixed valency of Co^{2+}/Co^{3+}. b) The Fe spectrum is very close to the standard sample of Fe_2O_3, indicating that the valence of Fe ions are all 3+ in the SRO–CFO nanostructure. c) The Ru spectrum exhibits a splitting peak toward higher binding energy with respect to the pure $SrRuO_3$, indicating the mixed valency of Ru^{4+}/Ru^{5+} in this system.

region) and the blue dot (SRO region), respectively, as shown in the right side of Figure 3. The spectrum from the SRO region exhibits a strong Fe peak (the lower-right panel of Figure 3), indicating that Fe diffused into the SRO matrix during the film growth. Furthermore, the Co/Fe ratio in the CFO nanopillars is about 0.77 quantified from the EDS spectrum (the upper-right panel of Figure 3), which is higher than 1/2 (the ratio of standard CFO). Such Co-rich non-stoichiometry of CFO is consistent with the diffusion of Fe into the SRO matrix. Based on this result, we can also roughly estimate how many Fe ions escape from the $CoFe_2O_4$ nanopillars into the SRO matrix: The EDS shows Co/Fe = 0.77, or we can rewrite it as Co/Fe = 1/1.3, which means an average of 0.7 Fe ions per one $CoFe_2O_4$ dissolves into SRO. In this work, the CFO/SRO ratio has been designed as 0.33. Therefore, by multiplying these two values (0.7×0.33), we can obtain the Fe doping concentration in SRO, which is about 23%. The X-ray absorption spectroscopy (XAS) measurements at the Co-$L_{2,3}$, Fe-$L_{2,3}$, and Ru-L_3 edges were then performed to realize the electronic structural information and the valence of the Co, Fe, and Ru ions. As for the Co spectrum in the SRO–CFO nanostructures shown in **Figure 4**a, the profile compared with the standard sample of $LaCoO_3$ and CoO strongly suggests the presence of Co^{2+} and low-spin Co^{3+} ions in this system, where the main peaks of Co^{2+} and Co^{3+} are assigned at 779 and 780.7 eV, respectively.[29–31] The Fe-$L_{2,3}$ XAS results (Figure 4b) also establish that the valence of Fe ions are all 3+ in the SRO–CFO nanostructure. The Ru-L_3 peak shown in Figure 4c depicts that SRO–CFO is shifted toward a higher binding energy with respect to the pure $SrRuO_3$, indicating the mixed valency of Ru^{4+}/Ru^{5+} in this system. Several reports of doped SRO cases have illustrated that the substitution of a Ru site by 3d transition elements would cause the presence of Ru^{5+} and the suppression of itinerant Ru 4d electrons.[24–28] According to the results of EDS and XAS, the inter-diffused Fe^{3+} ions should be responsible for this carrier localization in the SRO matrix and the weakness of the Ru electronic mobility. The results of the Fe-doped SRO systems studied by Mamchik et al.[24] or Fan et al.,[26] indicated that the doped SRO behavior would change from metallic to semiconducting when the Fe doping concentration exceeds 15%. Since the Fe doping concentration is around 23% in our system, it exhibits a semiconducting transport behavior, which is consistent with the literature.

However, the key difference between doped SRO systems and the self-assembled heteroepitaxial nanostructures is the physical interactions between the matrix and nanopillars. In order to investigate the correlation between these magnetic CFO nanopillars and doped SRO matrix, the measurement of field-dependent resistivity curves was adopted. As shown in **Figure 5**a, we can note an obvious decrease of resistivity at around $T_{C,SRO}$ while applying a magnetic field. The following MR curves in Figure 5b exhibit a large negative MR (≈40%) which only requires a magnetic field of 0.5 T. A large MR mostly occurs in CMR materials such as doped manganites[32,33] or manganite-based nanocomposite systems.[10–13] The maximum MR at the transition temperature (i.e., metal-to-insulator transition temperature (T_{MI}) or Curie temperature (T_C)) is usually caused by the suppression of spin-flip scattering induced by magnetic ordering, which commonly exists in most ferromagnetic materials systems.[18–20,24–28] However, our system delivers an even more intriguing result that large MR can also be obtained in the composites composed of two materials without apparent MR behavior in their respective single phase states. It is also of interest that the SRO matrix in our system has around 23% Fe doping concentration and a semiconducting behavior, and according to the reports by *Mamchik* et al., Fe-doped SRO with this composition should present a gradually increasing MR with decreasing temperature instead of the presence of a turning point at around $T_{C,SRO}$.[24] Hence, the magnetic CFO nanopillars in this nanostructure system must play an important role to drive this phenomenon of the observed maximum MR.

The field-dependent MR curve operated at 150 K in Figure 5c and the hysteresis loops measured at different temperatures in

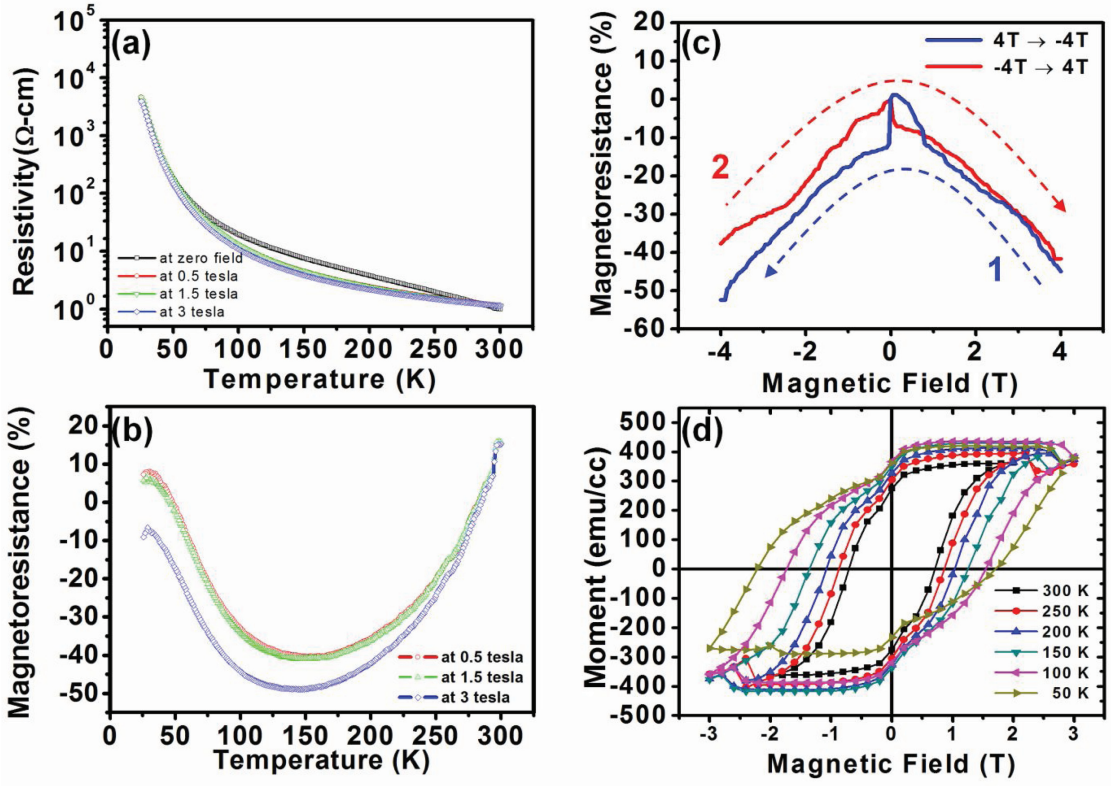

Figure 5. a) The temperature-dependent transport measurement performed at 0, 0.5, 1.5, and 3 T. b) The respective magnetoresistance of 0.5, 1.5, and 3 T extracted from (a) according to the equation: MR(%) = 100% × [$\rho(H) - \rho(0T)$]/$\rho(0T)$, where $\rho(H)$ and $\rho(0T)$ are the resistivity under magnetic field and a zero field, respectively. c) The field-dependent transport measurement operating at around $T_{C,SRO}$ shows a large MR effect in a field and a large MR in a higher field. The blue curve indicates that the magnetic field is applied from 4 to –4 T, and the red curve means from –4 to 4 T. d) The hysteresis loop measured at different temperatures shows an obviously decoupled feature below $T_{C,SRO}$.

Figure 5d help us to understand this mechanism further. The observed MR exhibits an asymmetric behavior that exists in either field from positive to negative (the blue curve 1) or vice versa (the red curve 2). A sudden drop of resistivity occurs at several hundred oersted (Oe) while the magnetic field is just changing direction in curve 1 or 2, which is similar to grain boundary tunneling MR observed in polycrystalline or obviously phase-separated single-crystalline manganites.[32–34] It may be caused by the suppression of spin scattering at the hetero-interfaces between CFO pillars and the SRO matrix while applying a weak magnetic field. Usually this phenomenon is highly correlated to the magnetic domain rotation; however, recalling the phase diagram proposed by *Mamchik et* al., 23% Fe-doped SRO is paramagnetic above ≈50 K, then becomes cluster glass (CG) between 25 and 50 K, and spin glass below 25 K.[24] This implies that no obvious ferromagnetic SRO domains exist at this temperature (≈150 K). The most possible origin of MR is that the spin localized Fe^{3+} in the SRO matrix should be responsible for interacting with the magnetic CFO pillars, and lead to the spin tunneling between these magnetic domains. The hysteresis loops measured at different temperatures in Figure 5d also support this hypothesis. The loops above $T_{C,SRO}$ maintain the feature of a nearly single ferromagnetic phase and enhanced magnetization, indicating that the spin localized Fe^{3+} in SRO has strong magnetic coupling with the CFO nanopillars. Nevertheless, those loops below 150 K clearly demonstrate that two decoupled ferromagnetic phases start to emerge and become more difficult to saturate even at a high field such as 4 T. The presence of soft and hard ferromagnetic phases is obviously from the doped SRO matrix and CFO nanopillars, respectively, and this soft phase should be in the CG or SG state, which belongs to the short range ferromagnetic ordering. It means that the magnetic state of chaos could be procured below $T_{C,SRO}$, which adds the opportunity of spin scattering and makes the resistivity rise to that of a nearly demagnetized state in the temperature-dependent measurements.

After integrating all the above, we propose a model as shown in **Figure 6** to describe the mechanism of the observed MR. In this system, CFO nanopillars possess a large magnetic anisotropy along the out-of-plane direction due to strong lattice coupling between CFO and SRO. On the other hand, the interdiffused Fe^{3+} ions from the CFO pillars in the SRO matrix would substitute Ru sites due to the close orbital energy level of Fe^{3+} and Ru^{4+}.[24,26] The electrons of the Fe^{3+} ions in SRO are usually localized and have a strong resonance with Ru^{4+}, leading to the spin polarization of neighboring Ru 4d electrons. These spin localized Fe^{3+} in SRO and Fe^{3+} in CFO have strong magnetic coupling above $T_{C,SRO}$, which can be evidenced by the

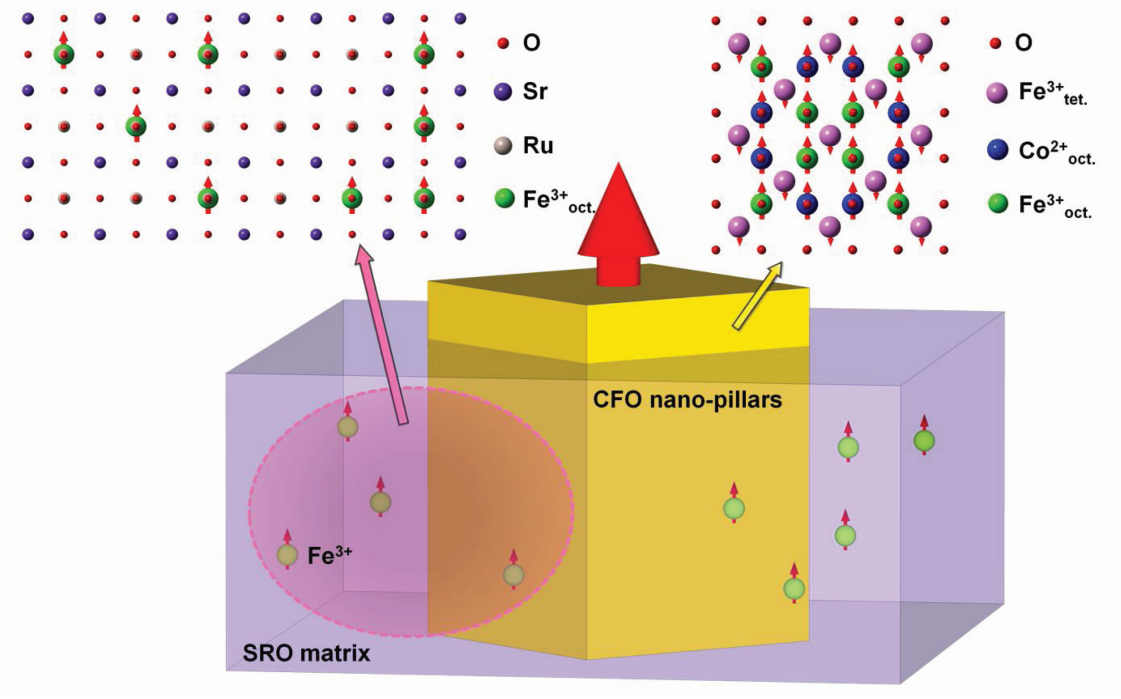

Figure 6. The depiction of the cause of large MR in this nanostructure system. The inter-diffused Fe ions and CFO nanopillars play a role to reduce the resistivity while they are put in a magnetic field. The aligned spins in Fe ions and magnetic moments in CFO nanopillars correspond to the suppression of magnetic scattering from ions and interfaces.

presence of a single-phase hysteresis loop. With the assistance of a magnetic field, polarized spins can pass through the localized Fe^{3+} ions and the interfacial boundaries of the CFO pillars more easily when they are aligned in the same direction, which results in the decrease of resistivity. In addition, this coupling is also competing with thermal energy so that enhanced magnetization can be observed as the temperature decreased. Therefore, a larger variation between zero field and field resistivity could be obtained expectedly as the temperature decreases. However, SRO becomes ferromagnetic CG or SG when the temperature decreases below $T_{C,SRO}$, leading to a decoupling effect between the SRO matrix and CFO nanopillars. It means that Fe^{3+} ions in SRO are only interacting with neighboring Ru ions instead of Fe^{3+} ions in CFO, and this magnetic disorder in the system below $T_{C,SRO}$ increases the opportunity of electron scattering. Hence, the difference between the zero field and field resistivity becomes smaller, and finally we can observe a maximum MR value occurring at around $T_{C,SRO}$. Based on this model, we are able to explain why this nanocomposite system consisting of two non-CMR materials can also lead to a great MR effect.

In summary, we have noticed that the composite CFO–SRO nanostructured thin film grown on a STO (100) substrate achieved a decrease of resistivity (≈40%) by only applying a field (0.5 T) around the Curie temperature of SRO. Both CFO and SRO are not CMR materials; however, their combination can exhibit an intriguing MR effect. To achieve this result, the crucial point is that we allow a small number of Fe ions from the CFO pillars to diffuse into the SRO matrix and substitute the Ru sites. The strongly coupled Fe^{3+} ions in the SRO matrix and CFO pillars above $T_{C,SRO}$ assist in lowering the resistivity while their magnetic moment are aligned in the same direction in a magnetic field due to the suppression of magnetic scattering from ions and interfaces. Below $T_{C,SRO}$, decoupled soft ferromagnetic SRO and hard ferromagnetic CFO enhance the magnetic scattering, and thus resistivity can not be effectively reduced by the magnetic field. Therefore, a maximum of MR value can be observed at $\approx T_{C,SRO}$. This is very interesting since we unexpectedly demonstrate that the large MR effect can be directly obtained by combining a magnetic material and a conductive material, and it provides potential to design or create a new kind of spintronic material system.

Experimental Section

Sample Fabrication: Dual-target systems of bulk $SrRuO_3$ (SRO) and bulk $CoFe_2O_4$ (CFO) discs mounted on a computer-controlled exchanging stage were used to fabricate epitaxial CFO–SRO self-assembled nanostructures on an STO substrate by pulsed laser deposition with a KrF (λ = 248 nm) excimer laser. The laser beam was focused on the target with an energy density of approximately 5 J cm^{-2} and repetition rate of 10 Hz. Samples were deposited at the substrate temperature of 750 °C and in a dynamic oxygen pressure of 100 mTorr. The ratio of CFO to SRO was modulated at about 0.33. After the thin-film growth, samples were cooled to room temperature at 20 °C min^{-1} in oxygen at ≈1 atm.

Characterization of Structure and Physical Properties: High-resolution XRD techniques were used to confirm the crystal quality of CFO–SRO nanostructures at beamline BL17A in the National Synchrotron Radiation Research Center (NSRRC), Taiwan. The microstructures of the sample were characterized by a Cs-corrected HAADF-STEM equipped with an EDS detector for chemical analyses (STEM; JEOL JEM2100F,

Cs-corrector; CEOS Gmbh). Analysis of the surface morphology (AFM) and the conducting SRO matrix (CAFM)in contact mode were performed using a Bruker Multimode VIII. The voltage was set at 1.2 V. The valency of Co, Fe, and Ru was studied using soft X-ray absorption spectra. The Co- and Fe-$L_{2,3}$ XAS spectra were recorded at the Dragon beamline of the NSRRC in Taiwan with an energy resolution of 0.25 eV. The Ru-L_3 XAS measurements were performed at the Taiwan NSRRC 15B beamline, equipped with a double Si(111) crystal monochromator delivering photons from 2 keV and up. The photon-energy resolution at the Ru-$L_{2,3}$ edges ($h\nu \approx 2.9$ keV) was set at 0.6 eV. The temperature-dependent and magneto-transport properties were determined by a quantum design physical property measurement system (PPMS) along the film surface using a standard four-probe method. The samples were cooled from room temperature to 20 K by closed cycle refrigeration. The contacts were made by bonding copper wires on the samples.

Acknowledgements

The work was supported by the National Science Council of Republic of China (under contract No. NSC-101-2119-M-009-003-MY2), Ministry of Education (grant No. MOE-ATU 101W961), and Center for Interdisciplinary Science at National Chiao Tung University. The authors thank Dr. Takeharu Kato and Mr. Ryoji Yoshida in JFCC for their help in TEM sample preparation. R.H. is supported by Shanghai Pujiang talents plan (Grant No. 11PJ1402900). C.-G.D. is supported by the NSFC (61125403) and PCSIRT.

Received: April 1, 2013
Revised: May 31, 2013
Published online: July 12, 2013

[1] J. Mannhart, D. G. Schlom, *Science* **2010**, *327*, 1607.
[2] H. Y. Hwang, Y. Iwasa, M. Kawasaki, B. Keimer, N. Nagaosa, Y. Tokura, *Nat. Mater.* **2012**, *11*, 103.
[3] H. Zheng, J. Wang, S. E. Lofland, Z. Ma, L. Mohaddes-Ardabili, T. Zhao, L. Salamanca-Riba, S. R. Shinde, S. B. Ogale, F. Bai, D. Viehland, Y. Jia, D. G. Schlom, M. Wuttig, A. L. Roytburd, R. Ramesh, *Science* **2004**, *303*, 661.
[4] Y. Zhang, C. Deng, J. Ma, Y. Lin, C.-W. Nan, *Appl. Phys. Lett.* **2008**, *92*, 062911.
[5] N. Dix, R. Muralidharan, J.-M. Rebled, S. Estrsdé, F. Peiró, M. Varela, J. Fontcuberta, F. Sánchez, *ACS Nano* **2010**, *4*, 4955.
[6] F. Zavaliche, T. Zhao, H. Zheng, F. Straub, M. P. Cruz, P. L. Yang, D. Hao, R. Ramesh, *Nano Lett.* **2007**, *7*, 1586.
[7] M. Murakami, K.-S. Chang, M. A. Aronova, C.-L. Lin, Ming H. Yu, J. Hattrick Simpers, M. Wuttig, I. Takeuchi, C. Gao, B. Hu, S. E. Lofland, L. A. Knauss, L. A. Bendersky, *Appl. Phys. Lett.* **2005**, *87*, 112901.
[8] H. Yang, H. Y. Wang, J. Yoon, Y. Q. Wang, M. Jain, D. M. Feldmann, P. C. Dowden, J. L. MacManus-Driscoll, Q. X. Jia, *Adv. Mater.* **2009**, *21*, 3794.
[9] S. A. Harrington, J. Zhai, S. Denev, V. Gopalan, H. Wang, Z. X. Bi, S. A. T. Redfern, S.-H. Baek, C. W. Bark, C.-B. Eom, Q. X. Jia, M. E. Vickers, J. L. MacManus-Driscoll, *Nat. Nanotechnol.* **2011**, *6*, 491.
[10] A. P. Chen, Z. X. Bi, C. F. Tsai, J. H. Lee, Q. Su, X. H. Zhang, Q. X. Jia, J. L. MacManus-Driscoll, H. Y. Wang, *Adv. Funct. Mater.* **2011**, *21*, 2423.
[11] L. Fei, L. Zhu, X. Cheng, H. Y. Wang, S. M. Baber, J. Hill, Q. Lin, Y. Xu, S. Deng, H. Luo, *Appl. Phys. Lett.* **2012**, *100*, 082403.
[12] Z. Bi, E. Weal, H. Luo, A. Chen, J. L. MacManus-Driscoll, Q. Jia, H. Y. Wang, *J. Appl. Phys.* **2011**, *109*, 054302.
[13] M. Staruch, D. Hires, A. Chen, Z. Bi, H. Wang, M. Jain, *J. Appl. Phys.* **2011**, *110*, 113913.
[14] H.-J. Liu, L.-Y Chen, Q. He, C.-W. Liang, Y.-Z. Chen, Y.-S. Chien, Y.-H. Hsieh, S.-J. Lin, E. Arenholz, C.-W. Luo, Y.-L. Chueh, Y.-C. Chen, Y.-H. Chu, *ACS Nano* **2012**, *6*, 6952.
[15] G. Koster, L. Klein, W. Siemons, G. Rijnders, J. S. Dodge, C.-B. Eom, D. H. A. Blank, M. R. Beasley, *Rev. Mod. Phys.* **2012**, *84*, 253.
[16] S. Jin, T. H. Tiefel, M. McCormack, R. A. Fastnacht, R. Ramesh, L. H. Chen, *Science* **1994**, *264*, 413.
[17] G. J. Snyder, R. Hiskes, S. DiCarolis, M. R. Beasley, T. H. Geballe, *Phys. Rev. B* **1996**, *53*, 14434.
[18] S. C. Gausepoh, M. Lee, K. Char, R. A. Rao, C. B. Eom, *Phys. Rev. B* **1995**, *52*, 3459.
[19] L. D. B. Kacedon, R. A. Rao, C. B. Eom, *Appl. Phys. Lett.* **1997**, *71*, 1724.
[20] M. Ziese, I. Vrejoiu, D. Hesse, *Phys. Rev. B* **2010**, *81*, 184418.
[21] A. V. Ramos, J.-B. Moussy, M.-J. Guittet, M. Gautier-Soyer, C. Gatel, P. Bayle-Guillemaud, B. Warot-Fonrose, E. Snoeck, *Phys. Rev. B* **2007**, *75*, 224421.
[22] W. Götz, N. M. Johnson, C. Chen, H. Liu, C. Kuo, W. Imler, *Appl. Phys. Lett.* **1996**, *68*, 667.
[23] S.-T. Lo, H.-E. Lin, S.-W. Wang, H.-D. Lin, Y.-C. Chin, H.-H. Lin, J.-C. Lin, C.-T. Liang, *Nanoscale Res. Lett.* **2012**, *7*, 640.
[24] A. Mamchik, I.-Wei Chen, *Phys. Rev. B* **2004**, *70*, 104409.
[25] A. Mamchik, W. Dmowski, T. Egami, I.-Wei Chen, *Phys. Rev. B* **2004**, *70*, 104410.
[26] J. Fan, S. Liao, W. Wang, L. Zhang, W. Tong, L. Ling, B. Hong, Y. Shi, Y. Zhu, D. Hu, L. Pi, Y. Zhang, *J. Appl. Phys.* **2011**, *110*, 043907.
[27] S. Zhang, S. Tan, L. Pi, C. Zhang, Y. Zhang, *J. Appl. Phys.* **2011**, *109*, 07E156.
[28] L. Pi, A. Maignan, R. Retoux, B. Raveau, *J. Phys.: Condens. Matter* **2002**, *14*, 7391.
[29] J.-G. Cheng, J.-S. Zhou, Z. Hu, M. R. Suchomel, Y. Y. Chin, C. Y. Kuo, H.-J. Lin, J. M. Chen, D. W. Pi, C. T. Chen, T. Takami, L. H. Tjeng, J. B. Goodenough, *Phys. Rev. B* **2012**, *85*, 094424.
[30] T. Burnus, Z. Hu, H. H. Hsieh, V. L. J. Joly, P. A. Joy, M. W. Haverkort, H. Wu, A. Tanaka, H.-J. Lin, C. T. Chen, L. H. Tjeng, *Phys. Rev. B* **2008**, *77*, 125124.
[31] C. H. Kim, Y. Myung, Y. J. Cho, H. S. Kim, S.-H. Park, J. Park, J.-Y. Kim, B. Kim, *J. Phys. Chem. C* **2009**, *113*, 7085.
[32] H. Y. Hwang, S.-W. Cheong, N. P. Ong, B. Batlogg, *Phys. Rev. Lett.* **1996**, *77*, 2041.
[33] R.-W. Li, Z.-H. Wang, W.-N. Wang, J.-R. Sun, Q.-A. Li, S.-Y. Zhang, Z.-H. Cheng, B.-G. Shen, B.-X. Gu, *Appl. Phys. Lett.* **2002**, *80*, 3367.
[34] K.-I. Kobayashi, T. Kimura, H. Sawada, K. Terakura, Y. Tokura, *Nature* **1998**, *395*, 677.